Check for updates

Synthesis, characterization, and application of ternary CuO/ZrO$_2$@S-doped g-C$_3$N$_4$ hybrid nanocomposites†

Nigussie Alebachew, [ID] *[ab] Taye B. Demissie, [ID] *[c] H. C. Ananda Murthy, [ID] [de] Bedasa Abdisa Gonfa, [ID] [b] Karel G. von Eschwege, [ID] [f] Elizabeth Coetsee, [ID] [g] Ernst H. G. Langner, [ID] [f] Jayadev[h] and B. H. Doreswamy[i]

Graphitic carbon nitride (g-C$_3$N$_4$) is utilized across various fields, including catalysis, hydrogen production, and biosensing, due to its basic surface sites. However, g-C$_3$N$_4$ often shows limited efficiency in such applications, mainly due to challenges related to absorption and low conductivity. This study aimed to synthesize S-doped g-C$_3$N$_4$/CuO/ZrO$_2$-based semiconducting ternary nanocomposites (NCs) for catalytic applications using a chemical precipitation method. A straightforward gas-templating technique was applied to achieve one-step nano-structuring of S-doped g-C$_3$N$_4$ at 550 °C. The interactions between cubical CuO structures, monoclinic ZrO$_2$, and flower-like S-doped g-C$_3$N$_4$ morphologies were investigated using a range of analytical techniques, including X-ray diffraction (XRD), high-resolution X-ray photoelectron spectroscopy (HR-XPS), high-resolution scanning electron microscopy (HR-SEM), transmission electron microscopy (TEM), Fourier transform infrared (FTIR) spectroscopy, ultraviolet-visible (UV-Vis) diffuse reflectance spectroscopy (DRS), thermogravimetric analysis (TGA), differential thermal analysis (DTA), Brunauer−Emmett−Teller (BET) surface area analysis, and photoluminescence (PL) studies. The superior performance of CuO/ZrO$_2$@$_2$S-doped g-C$_3$N$_4$ (30%) nanocomposite is attributed to its smaller crystalline size, optimized band gap energy, and large surface area. These features collectively enhance electron−hole pair separation efficiency and increase the number of active sites for adsorption and reaction. Such improvements not only enhance sensitivity but also boost sensor efficiency through better charge carrier generation, selective detection capabilities, and facilitated charge transfer. These enhancements also contribute to reducing recombination losses and accelerating signal generation and g-C$_3$N$_4$ transport. These synthesized ternary NCs were applied to bisphenol A (BPA) detection. The electrocatalytic behaviour of the modified carbon paste electrode (CPE) was assessed by measuring BPA *via* cyclic voltammetry (CV) under ideal conditions (pH 5). The CuO/ZrO$_2$@S-doped g-C$_3$N$_4$ (30%)/CPE system demonstrated high electrocatalytic performance, achieving reproducibility with a 1.7 μM detection limit and 2.1 μM limit of quantification. Overall, this research highlights the potential of synthetic ternary NCs as versatile materials for environmental remediation applications.

[a]Department of Chemistry, College of Natural and Computational Science, Wolkite University, Wolkite, P. O. Box 07, Ethiopia. E-mail: nigussie.alebachew@wku.edu.et

[b]Department of Applied Chemistry, College of Natural and Computational Science, Adama Science and Technology University, P. O. Box 1888, Adama, Ethiopia. E-mail: nigussiealebachew@gmail.com; bedassa.abdissa@astu.edu.et

[c]Department of Chemistry, University of Botswana, P/Bag 00704, Gaborone, Botswana. E-mail: demissiet@ub.ac.bw

[d]Department of Applied Sciences, Papua New Guinea University of Technology, Lae, Morobe Province, 411, Papua New Guinea. E-mail: anandkps350@gmail.com

[e]Department of Prosthodontics, Saveetha Dental College & Hospital, Saveetha Institute of Medical and Technical Sciences (SIMATS), Saveetha University, Chennai-600077, Tamil Nadu, India

[f]Department of Chemistry, University of the Free State, P. O. Box 339, Bloemfontein, South Africa. E-mail: veschwkg@ufs.ac.za; langneeh@ufs.ac.za

[g]Department of Physics, University of the Free State, P. O. Box 339, Bloemfontein, South Africa. E-mail: coetseee@ufs.ac.za

[h]Department of Chemistry, SJB Institute of Technology, Bengaluru, 560060, India. E-mail: devbcv@gmail.com

[i]Department of Physics, SJB Institute of Technology, Bengaluru, 560060, India. E-mail: dorephy@gmail.com

† Electronic supplementary information (ESI) available: High resolution spectra for S 2p for CuO/ZrO$_2$@S-doped g-C$_3$N$_4$ NC, XRD pattern of CuO/ZrO$_2$@S-doped g-C$_3$N$_4$, CuO and ZrO$_2$, M–S curves and physicochemical properties of the synthesized samples, comparison between proposed band structure of CuO/ZrO$_2$@S-doped g-C$_3$N$_4$ and its components. See DOI: https://doi.org/10.1039/d4ra08941c

1. Introduction

Water contamination is largely driven by the rapid growth of industrial activities. Among the hazardous chemicals contributing to this issue, bisphenol A (BPA) stands out due to its extensive production for applications primarily in polycarbonate plastics, epoxy resins, and thermal paper products. BPA is present in a wide range of items, including impact-resistant windows, eyewear, reusable water bottles, bottle caps, and water supply piping systems.[1] Exposure to these chemicals has been associated with gestational length and several growth parameters at birth, including birth weight and birth length[2] as well as cognitive disorders.[3] Overall, evidence supports the notion of an increased risk of adverse effects due to exposure to high concentrations of BPA and other chemicals.[4,5] In relation to this, modifying the existing methods for monitoring and detecting the levels of BPA is still at an early stage. Therefore, the development of novel nanocomposites with high sensitivity and detection of BPA at low concentration is crucial.[6] Besides this, most of the methods used for the removal of such chemicals require complicated sample preparation and pre-treatment, high-cost instruments and skilled manpower.[3,7]

In contrast to other semiconductors, g-C$_3$N$_4$ has promising electrical and morphological properties, and has great thermal stability up to 600 °C. However, the widespread use of g-C$_3$N$_4$ in photocatalysis, sensors and reduction reactions is eventually hampered by various intrinsic properties, such as low quantum efficiency, small specific surface area, and quick recombination of photogenerated electron–hole pairs.[8–10] Several techniques have been implemented to improve the catalytic performance of g-C$_3$N$_4$ by utilizing various manufacturing processes. Doping with nonmetal elements such as nitrogen,[9] oxygen,[11] and sulfur[12] exhibited significant opportunity to increase the ability to absorb visible light by g-C$_3$N$_4$. However, when two or more semiconductors are combined, the combined semiconductors' properties are improved over those of the constituent semiconductors.[13] For instance, several studies investigated the loading of transition metal oxides like ZnO,[14] CuO,[15] and Fe$_2$O$_5$,[16] which significantly boosted the potential dangerous organic pollutants detection and degradation rates of g-C$_3$N$_4$ based NCs.

CuO, a p-type semiconductor, is favored for its adaptable electrical structure, narrow bandgap, low cost, and eco-friendly synthesis. However, its photocatalytic efficiency is limited by low light absorption and rapid electron–hole recombination.[17] In contrast, ZrO$_2$ offers superior mechanical strength, high ionic conductivity, low thermal conductivity, and excellent thermal stability, making it a popular alternative.[18] Additionally, ZrO$_2$ is a promising candidate for various applications due to its unique characteristics, including a high surface area and the presence of abundant oxygen vacancies. These features make it suitable for use as solid-state electrolytes, thermal barrier coatings, electro-optical materials, and as a catalyst or catalyst support,[8,19] and sensor technology.[20] ZrO$_2$, on the other hand, presents difficulty in decreasing its broad band gap energy (>3.5 eV), which restricts its application in photocatalysis, particularly in UV-Vis applications.[21] As a result, new multi-functional semiconducting ternary NCs based on g-C$_3$N$_4$ has to be manufactured to improve the aforementioned environmental issues as well as employing novel materials and processes. g-C$_3$N$_4$ can easily be prepared via one-step polymerization of cheap feed stocks such as melamine,[22] cyanamide,[23] dicyanamide,[24] or thiourea.[25] Different techniques have been employed to improve the limitations of g-C$_3$N$_4$. For example, some researchers synthesized metal oxide incorporated g-C$_3$N$_4$ NCs via precipitation,[26,27] impregnation and hydrothermal[28] methods. However, due to limitations in yield and energy consumption, the simplest and familiar calcination method is recommended. At present, direct pyrolysis of precursors, followed by ultrasonication and chemical precipitation, is considered as the most efficient synthesis method for g-C$_3$N$_4$-based nanocomposites due to its cost-effectiveness, simplicity, and high yield. Fig. 1 show the preparation and application processes used in this study.

The ternary CuO/ZrO$_2$@S-doped g-C$_3$N$_4$ nanocomposites were prepared through a straightforward pyrolysis approach that integrates chemical precipitation and pyrolysis methods. Employing advanced analytical techniques, this work establishes a foundation for future synthesis, characterization, and potential applications of ternary semiconducting heterostructures. To the best of our knowledge, this is the first report detailing the synthesis of ternary nanocomposites comprising sulphur-doped graphitic carbon nitride, copper oxide, and zirconia for versatile applications.

2. Experimental details

2.1 Chemicals and reagents

The chemicals and reagents utilized in this study include urea (CO(NH$_2$)$_2$), ammonium sulphate ((NH$_4$)$_2$SO$_4$), absolute ethanol (CH$_3$CH$_2$OH, 97%), sulfuric acid (H$_2$SO$_4$), sodium hydroxide (NaOH), aqueous ammonia (NH$_3$(OH)), zirconium oxychloride (ZrOCl$_2$·8H$_2$O), copper nitrate (Cu(NO$_3$)$_2$·3H$_2$O), hydrochloric acid (HCl, 98%), and bisphenol A (BPA), all sourced from Sigma-Aldrich. All reagents were of analytical grade and were used as received, without additional purification.

2.2 Synthesis of sulphur doped graphite carbon nitride (S-doped g-C$_3$N$_4$)

S-Doped g-C$_3$N$_4$ NC was prepared by applying previously reported method, with enhanced gas templating method.[29,30]

2.3 Synthesis of CuO/ZrO$_2$@S-doped g-C$_3$N$_4$ NCs

Ternary CuO/ZrO$_2$@S-doped g-C$_3$N$_4$ NCs were prepared by employing a simple chemical precipitation method. In a typical synthesis, a mixture of C$_2$H$_5$OH and S-doped g-C$_3$N$_4$ was sonicated for 2 h, labelled as solution "A". Applying a chemical precipitation technique, the CuO solution was prepared from the desired amount of Cu(NO$_3$)$_2$·3H$_2$O (3.77 g), labelled as solution "B". Similarly, ZrOCl$_2$·8(H$_2$O)·3H$_2$O (3.25 g) was prepared and labelled as solution "C". To prepare ternary powder sample, both solutions "A" and "B" were added to
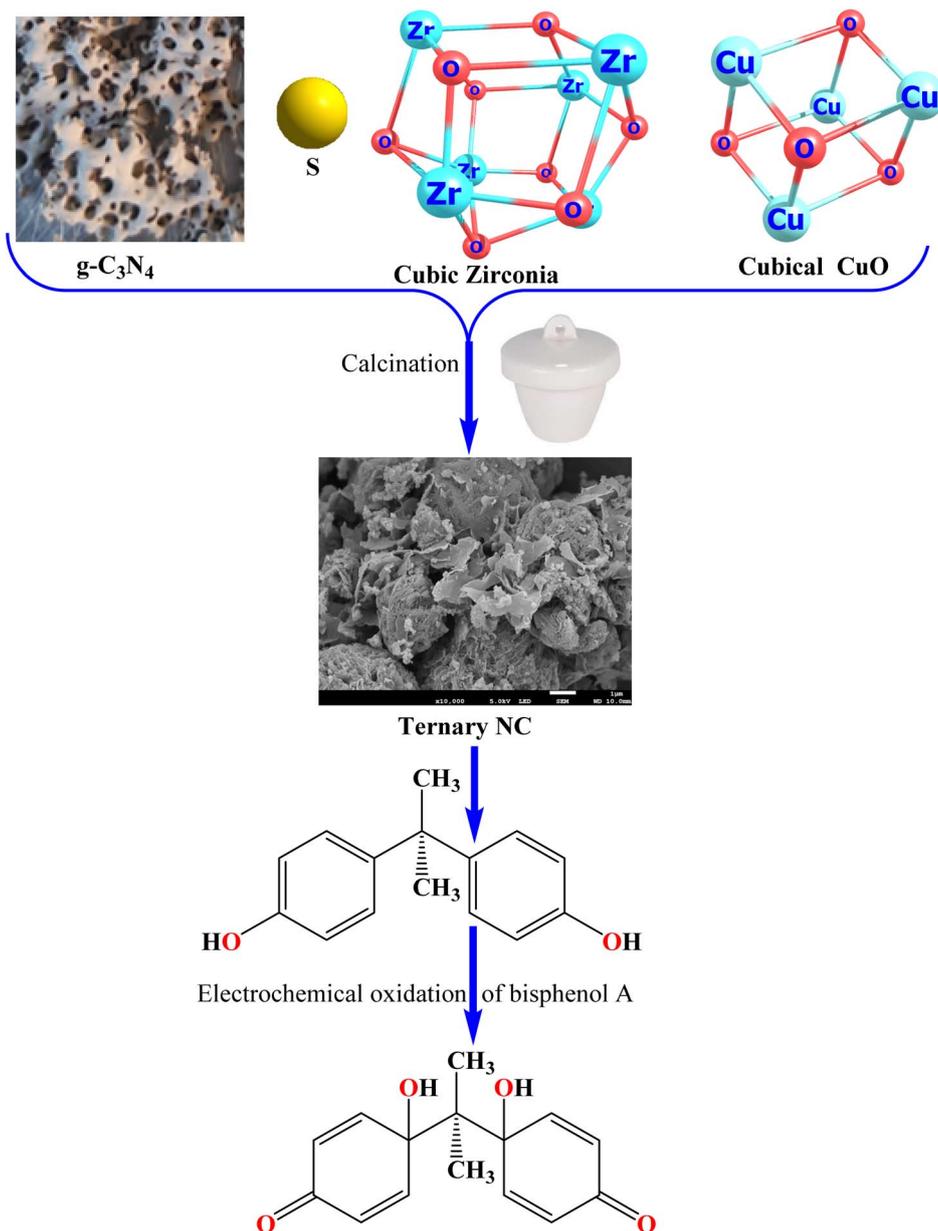
Fig. 1 Schematic illustration for preparation and application processes.

solution "C" and the mixture was stirred for 4 h, while adding deionized water until the pH reached approximately 10. After filtering and repeatedly washing with deionized water and ethanol (98%), the mixture was dried in an oven at 180 °C overnight. After grinding, the sample was placed in a muffle furnace at 500 °C and heated at a rate of 5 °C min⁻¹ for 3 h. In previous studies,[10,30,31] it was noticed that S-doped g-C₃N₄ is stable at 500 °C. After allowing the furnace to cool, the resulting ternary CuO/ZrO₂@S-doped g-C₃N₄ powder sample was obtained. Following similar experimental conditions, the remaining ternary CuO/ZrO₂@S-doped g-C₃N₄ (5%), CuO/ZrO₂@S-doped g-C₃N₄ (10%) and CuO/ZrO₂@S-doped g-C₃N₄ (20%) NCs and CuO/ZrO₂@S-doped g-C₃N₄ (30%) powder samples were prepared.

2.4 Materials characterization

The synthesized samples were analysed using a suite of advanced instrumental techniques. The phase structure was identified *via* powder X-ray diffraction (XRD) using a Cu Kα radiation target (40 kV, 30 mA) at a scanning rate of 3° min⁻¹ with a SHIMADZU XRD-7000 diffractometer. Sample purity was assessed by Fourier transform infrared (FTIR) spectroscopy on a PerkinElmer Spectrum 65 in the 4000–400 cm⁻¹ range (resolution: 4 cm⁻¹, 4 scans) using KBr pellets. Optical properties were explored through UV-Vis diffuse reflectance spectroscopy (DRS) with a PerkinElmer Lambda 950 spectrometer and BaSO₄ integrating sphere over a wavelength range of 200–800 nm. Thermal stability was evaluated using capillary tubes and a digital melting point apparatus, while thermogravimetric analysis (TGA) and differential thermal

analysis (DTA) were performed with a DTG-60H Shimadzu thermal analyser under an N_2 atmosphere (20 mL min^{-1}) and a heating rate of 15 °C min^{-1}, spanning from room temperature to 1000 °C. Photoluminescence (PL) spectra were acquired on a Cary Eclipse fluorescence spectrophotometer with 324 nm excitation, using a xenon flash lamp.

To visualize the morphology, energy-dispersive X-ray spectroscopy (EDS), selected area electron diffraction (SAED), and high-resolution scanning electron microscopy (HR-SEM) using a JEOL 7800F SEM were employed, along with high-resolution transmission electron microscopy (HRTEM) performed on a JEOL TEM 2100. Chemical composition was analysed through X-ray photoelectron spectroscopy (XPS) using a PHI 5000 Versaprobe. Surface area and porosity were assessed using the Brunauer–Emmett–Teller (BET) method with a Micromeritics ASAP 2020 analyser and ASAP 2020 v2.0 software. These methods align with previous studies and have been validated for reliability.[30]

2.5 Electrochemical sensor test studies

2.5.1 Preparation of carbon paste-modified sensors for BPA detection. To evaluate the synthesized semiconductors' performance, g-C_3N_4, S-doped g-C_3N_4 and ternary CuO/ZrO$_2$@S-doped g-C_3N_4 NCs carbon pastes were modified to detect BPA in aqueous solution. Briefly, to prepare g-C_3N_4/CPE, S-doped g-C_3N_4/CPE and CuO/ZrO$_2$@S-doped g-C_3N_4/CPE sensors, a mixture of 0.455 g of graphite powder, 0.025 g of synthesized NCs, and 0.4 mL of paraffin oil was blended by hand, mixed in a mortar and pestle, and then inserted in the bottom of a plastic tube syringe (internal radius: 2 mm and 10 cm long). Electrical contact was performed by pushing a conductive copper wire into the end of the glass tube to stick to the carbon paste. When a fresh electrode surface was required, the new surface was generated by rapidly extruding a small plug of the carbon paste with a stainless-steel rod and smoothing the resulting surface on white paper.

2.5.2 Preparation of BPA solution. A 0.5 mM stock solution of BPA was prepared by dissolving 70 mg of BPA in 100 mL of distilled water, then further diluting this to a total volume of 1000 mL in a volumetric flask. From the stock solution, a range of BPA working solutions were freshly prepared by diluting with 10 mL of phosphate buffer solution (PBS) at pH 7.0. All solutions were made with double distilled water, and measurements were performed at room temperature (25 ± 5 °C).[30]

2.6 Density functional theory (DFT) calculations

The DFT calculations were performed using Gaussian 16 program package[32] and the B3LYP[33–35] functional together with 6-311++G(d,p) basis sets[36] and Grimme's dispersion[37] correction. All the optimized geometries were confirmed to be real minima by ensuring that there are no imaginary vibrational frequencies.

3. Results and discussion

3.1 Crystal structure, phase, and purity analysis

Fig. 2 shows the XRD patterns of g-C_3N_4, S-doped g-C_3N_4, CuO/ZrO$_2$@S-doped g-C_3N_4 (5, 10, 20 and 30%) NCs and pure CuO

Fig. 2 XRD pattern (top) and FT-IR (bottom) of g-C_3N_4 and S-doped g-C_3N_4, CuO/ZrO$_2$@S-doped g-C_3N_4 (5, 10, 20, and 30%) NCs, pure CuO and pure ZrO$_2$ NPs.

and ZrO$_2$ NPs. Two prominent peaks for g-C_3N_4 and S-doped g-C_3N_4 were observed. The distinctive graphitic structure of g-C_3N_4 is indicated by the high peak at $2\theta = 26.99°$ and the low intensity peak at $2\theta = 13.4°$, which are both attributed to (100) and (002) diffraction planes, respectively.[38] Compared to g-C_3N_4, the prominent peak for S-doped g-C_3N_4 appears sharper and more intense, suggesting an increased crystallinity. Additionally, the 2θ values and the main peak of S-doped g-C_3N_4 were observed to shift slightly to lower angles, with peaks at $2\theta = 23.98°$ (Table S1†) and $2\theta = 26.99°$, indicating the presence of impurities introduced by sulphur doping. The diffraction patterns confirmed that the fundamental structure of g-C_3N_4 remains unchanged in S-doped g-C_3N_4 sheets, consistent with previous studies.[39] No significant diffraction peaks of the CuO and ZrO$_2$ phases were observed in the ternary CuO/ZrO$_2$@S-doped g-C_3N_4 (5, 10, 20 and 30%) NCs samples through XRD examination. This may be due to the presence of small amounts of CuO and ZrO$_2$ NPs in the ternary NC, which could not be synchronized by the XRD instrument.[8] However, the presence of CuO and ZrO$_2$ NPs were confirmed by HRSEM, TEM, and XPS studies. For comparison, when the amounts of CuO and ZrO$_2$
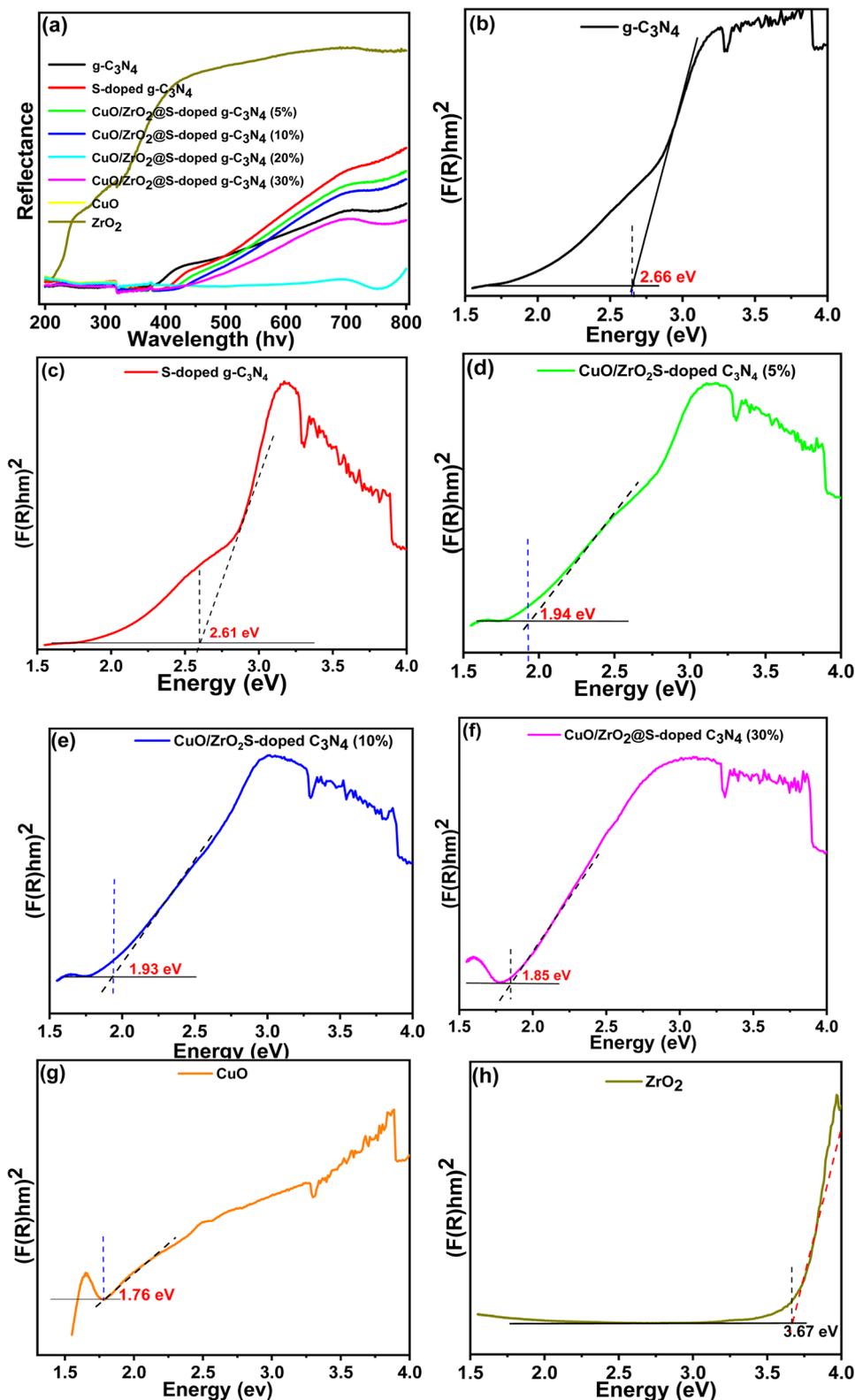
Fig. 3 Diffuse reflectance absorption spectra (a) and optical band gap plot transformed by the Kubelka–Munk function (b–h) of pristine g-C$_3$N$_4$, S-doped g-C$_3$N$_4$, CuO/ZrO$_2$@S-doped g-C$_3$N$_4$ (5%), CuO/ZrO$_2$@S-doped g-C$_3$N$_4$ (10%), CuO/ZrO$_2$@S-doped g-C$_3$N$_4$ (30%) NCs, pure CuO, and pure ZrO$_2$.

NPs were increased, the major peaks of S-doped g-C$_3$N$_4$, CuO and ZrO$_2$ became clearly visible, suggesting deposition of both CuO and ZrO$_2$ NPs under similar experimental conditions (see Fig. S1†). The two XRD patterns of Fig. 1 indicate no change in the basic structure of S-doped g-C$_3$N$_4$, which is in agreement with a previous report.[8,39]

The average crystallite sizes of the g-C$_3$N$_4$, S-doped g-C$_3$N$_4$, CuO/ZrO$_2$@S-doped g-C$_3$N$_4$ (5, 10, 20 and 30%) NCs and pure CuO and ZrO$_2$ NPs were found to be 5.52, 13.23, 13.23, 17.53, 5.80, 3.36, 30.09 and 13.10 nm, respectively, as presented in Table S1.† By considering the presence of the skeleton structure of the ternary NCs, the CuO and ZrO$_2$ NPs amount optimization was conducted by increasing the total amounts of the two metal oxides (5–30%). As shown in Table S1,† the crystal size of CuO/ZrO$_2$@S-doped g-C$_3$N$_4$ NCs is smaller (3.36 nm) than single g-C$_3$N$_4$ (5.52 nm), S-doped g-C$_3$N$_4$ (13.23 nm), CuO (30.09 nm) and ZrO$_2$ (13.10 nm). Cleary, this shows that, increasing the amounts of CuO and ZrO$_2$ NPs, the approximate crystalline size of ternary NCs decreased from 13.23 nm to 3.36 nm. This confirms the synergistic effect of the metallic NPs with the host S-doped g-C$_3$N$_4$, which is consistent with similar studies reported earlier.[40] Additionally, the full width at half maximum (FWHM) of the ternary NCs is broader than that of the binary NCs, aligning with the principle that smaller crystallite sizes lead to broader FWHM values. Complementing the XRD analysis, FT-IR spectroscopy was performed to examine surface functional groups and chemical bonding characteristics within the synthesized NCs. The FT-IR spectra for S-doped g-C$_3$N$_4$, CuO, ZrO$_2$, and CuO/ZrO$_2$@S-doped g-C$_3$N$_4$ (at 5%, 10%, 20%, and 30%) NCs are presented in Fig. 2.

The spectrum of S-doped g-C$_3$N$_4$ shows absorption bands at 1572 and 1645 cm^{-1}, which are attributable to the –C=N stretching vibration modes, while the peaks at 1241, 1319, 1404 cm^{-1} and 1649 cm^{-1} are due to the aromatic –C–N stretching frequency of heptazine derivatives. The peak at 805 cm^{-1} is related to the s-triazine ring modes which are associated with the condensed CN heterocycles. Sulphur doping was revealed by the peak at 705 cm^{-1}, which is attributed to the –C–S stretching vibration.[14] For pure ZrO$_2$, the absorption peaks at 509 cm^{-1} and 745 cm^{-1} are attributed to the stretching vibrations of –Zr–O. The peak at 537 cm^{-1} is the stretching vibrational band of the –Cu–O bond in monoclinic CuO crystal.[41] It is important to notice that the phases of both CuO and ZrO$_2$ NPs could not be detected in the given ratio in the NC. The shifting of the major peak in S-doped g-C$_3$N$_4$ in CuO/ZrO$_2$@S-doped g-C$_3$N$_4$ NCs positively indicates the incorporation of impurities, which in this case are CuO and ZrO$_2$.[42,43]

3.2 Optical property analysis

UV-Vis diffuse reflectance spectra were used to evaluate the bandgaps (E_g) of g-C$_3$N$_4$, S-doped g-C$_3$N$_4$, CuO/ZrO$_2$@S-doped g-C$_3$N$_4$ NCs, CuO and ZrO$_2$ samples. With the loading of S, CuO and ZrO$_2$, as compared to pristine g-C$_3$N$_4$, a broad absorption band with a red shift in the hybrid NCs appears from 450 nm to near 700 nm. This is attributed to structural defects formed in the NCs that was treated at a given temperature, illustrating easy incorporation of the impurities, S, CuO and ZrO$_2$, in the g-C$_3$N$_4$.

Using the band-gap energy relationship ($E_g = 1240/\lambda_g$)[44] and Kubelka–Munk function,[45] the variations of all band gaps are displayed in Fig. 2. The cut line method, which involves drawing a tangent and a horizontal line parallel to the baseline, was employed to identify the absorption wavelength threshold. The optical band gap energies (E_g) of the synthesized samples were calculated using the Kubelka–Munk equation. Diffuse reflectance (R) was determined using eqn (1).[45]

$$F(R) = \frac{(1-R)^2}{2R} \tag{1}$$

To obtain E_g, the Kubelka–Munk function was used, as represented by eqn (2).

$$(F(R)\hbar v)^n = A(\hbar v - E_g) \tag{2}$$

Here, λ represents the wavelength of the light source, and A is a constant influenced by the transition probability, which relates to the effective masses of carriers in the valence and conduction bands. The parameter n is a power index that corresponds to the optical absorption process and depends on the nature of electronic transitions within the semiconductor. For directly allowed transitions, n is set to 1/2. Additionally, $\hbar$ denotes Planck's constant; v is the light frequency, and E_g represents the energy gap between the conduction band (CB) minimum and the valence band (VB) maximum.

From the corresponding K–M plots (Fig. 3), the obvious change in E_g was observed with increasing percentage of CuO and ZrO$_2$ NPs, resulting in further narrowing of the band gap from 2.66 eV of g-C$_3$N$_4$ to 1.85 eV of CuO/ZrO$_2$@S-doped g-C$_3$N$_4$ NCs (30%) (see Table S1†). This could be attributed to shifting to the visible range by doping-induced modification in the lattices and structure of the S-doped g-C$_3$N$_4$ layers that is observed for Cu/ZrO$_2$@S doped g-C$_3$N$_4$ NCs.[44,46] This shows that it is possible to suitably tune the band gap with the incorporation of CuO and ZrO$_2$ NPs in the S-doped g-C$_3$N$_4$ host.

Fig. 4a and b display the photoluminescence (PL) intensities of pristine g-C$_3$N$_4$, S-doped g-C$_3$N$_4$, CuO, and ZrO$_2$ samples, which are higher than the PL intensity of the ternary NCs shown in Fig. 4b. This indicates an optimized electron/hole recombination rate in the ternary NCs. Notably, CuO/ZrO$_2$@S-doped g-C$_3$N$_4$ (5%) exhibits a higher PL intensity compared to the 10%, 20%, and 30% CuO/ZrO$_2$@S-doped g-C$_3$N$_4$ samples (Fig. 4b), suggesting a shorter charge carrier lifespan due to faster recombination.

In contrast, the PL intensity decreases for CuO/ZrO$_2$@S-doped g-C$_3$N$_4$ (20%) NC, possibly due to surface defects. However, the increased PL intensity observed with higher ZrO$_2$ and CuO content suggests an enhanced recombination centre in CuO/ZrO$_2$@S-doped g-C$_3$N$_4$ (30% and 20%) NCs. This is an indication for the presence of larger number of photon-activated sites on the ternary NCs. This also implies that the ternary CuO/ZrO$_2$@S-doped g-C$_3$N$_4$ NCs demonstrate a superior capability to separate photo-generated charge carriers compared to binary CuO@S-doped g-C$_3$N$_4$ (ref. 47) and ZrO$_2$@S-doped g-C$_3$N$_4$ NCs,[48] which is advantageous for the planned applications.

3.3 Thermal stability analysis

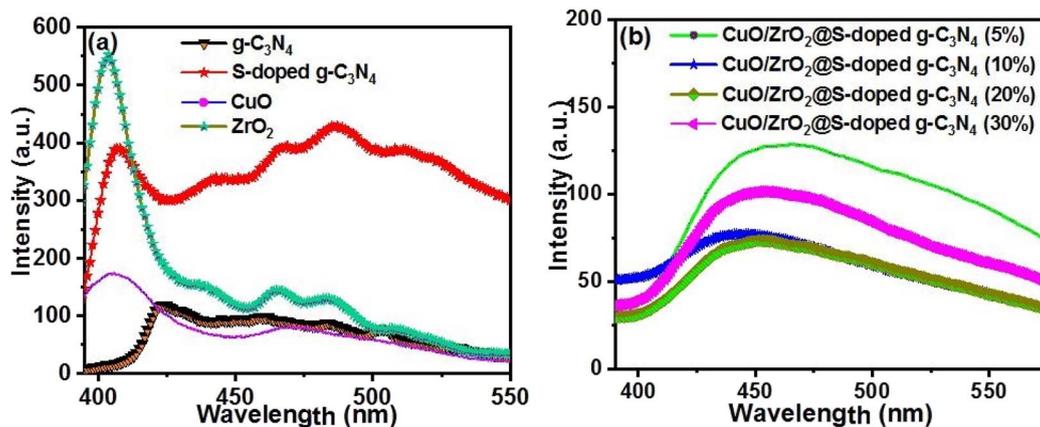The thermal stabilities of the S-doped g-C$_3$N$_4$ and CuO/ZrO$_2$@S-doped g-C$_3$N$_4$ samples were investigated from the precursors

Fig. 4 PL of (a) pristine g-C_3N_4, S-doped g-C_3N_4, CuO, and ZrO_2 NCs and (b) CuO/ZrO_2@S-doped g-C_3N_4 NCs.

before calcination by TGA/DTA technique under an N_2 atmosphere. The thermal stability property of the precursors ($CO(NH_2)_2$, $(NH_4)_2SO_4$, $ZrOCl_2 \cdot 8H_2O$, and $Cu(NO_3)_2 \cdot 3H_2O$) was studied by thermogravimetric analysis (TGA). It was used to investigate the thermal stability property of the precursors to synthesize ternary material. The DTA curve presented in Fig. 5a reveals an endothermic transformation at 132.19, 237.51 and 380.91 °C. The isomerization, which is the decomposition reaction of urea and ammonium sulphate, which also occurs as the weight loss rate increases to its maximum, which produces gases that will overflow and may absorb heat from the system.

The TGA curve for $CO(NH_2)_2$ and $(NH_4)_2SO_4$ (Fig. 5a, blue line), demonstrates progressive four weight loss steps that include the evaporation of adsorbed water molecules, the breakdown of NO_3 from $(NH_4)_2SO_4$ and/or the breakdown of amorphous parts of $CO(NH_2)_2$, and finally the decomposition of the crystalline part to produce carbon, nitrogen, sulphur, hydrogen, and ash, above 400 °C. Afterwards, the remaining portion of $CO(NH_2)_2$ and $(NH_4)_2SO_4$ are decomposed very slowly up to higher temperature. Thus, considering the DTA property (Fig. 5a) and similar previous studies,[30,31] the temperature at 550 °C was selected for the synthesis of S-doped g-C_3N_4.[47]

As seen in Fig. 5b, the TGA curve begins to stabilize around 400 °C, which is caused by mixing of the precursors, $Cu(NO_3)_2 \cdot 3H_2O$ and $ZrOCl_2 \cdot 8H_2O$. From the TGA/DTA results it is observed that the total decomposition temperature of the precursors ends at >520 °C. 500 °C was therefore chosen for the synthesis of ternary samples by taking into account the thermal stability of the precursors.[49]

3.4 Morphology and composition analyses

The HR-SEM/EDS technique (Fig. 6) was used to examine the morphology and elemental composition of both the inner and outer surfaces of the synthesized heterostructured g-C_3N_4, S-doped g-C_3N_4, and CuO/ZrO_2@S-doped g-C_3N_4 NCs. This approach offered detailed insights into the size, shape, elemental distribution, crystallography, and other physical and chemical characteristics through highly magnified imaging.
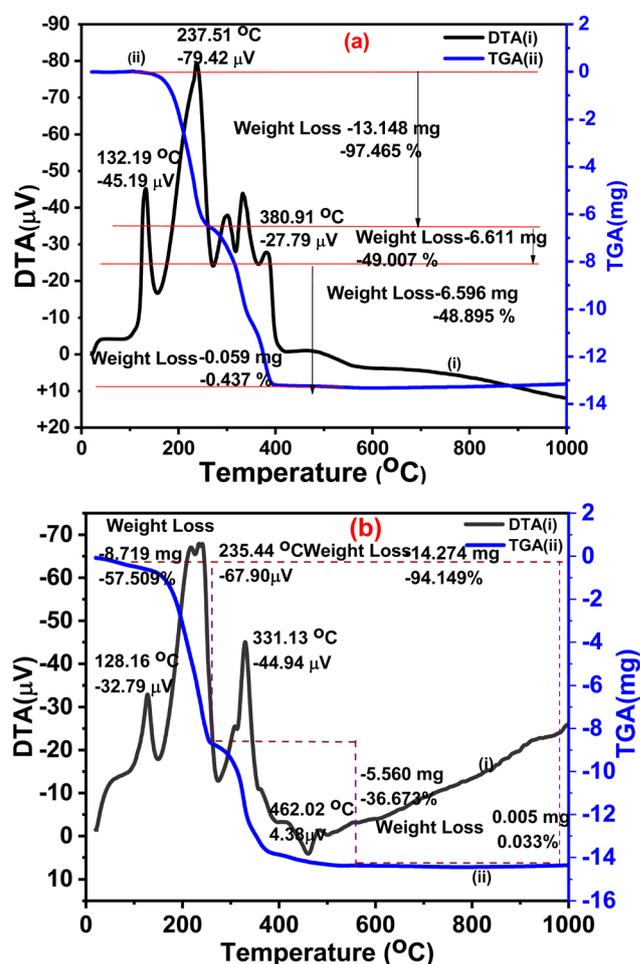

Fig. 5 TGA (blue)/DTA (black) thermogram for mixture of precursors (a) $CO(NH_2)_2$, and $(NH_4)_2SO_4$. (b) $CO(NH_2)_2$, $(NH_4)_2SO_4$, $Cu(NO_3)_2 \cdot 3H_2O$ and $ZrOCl_2 \cdot 8H_2O$ before calcination.

The HR-SEM image of g-C_3N_4 at various magnifications reveals maximum porosity, specific surface area (Table S1†), an amorphous structure, and irregularly formed particles, consistent with findings in other studies.[41]
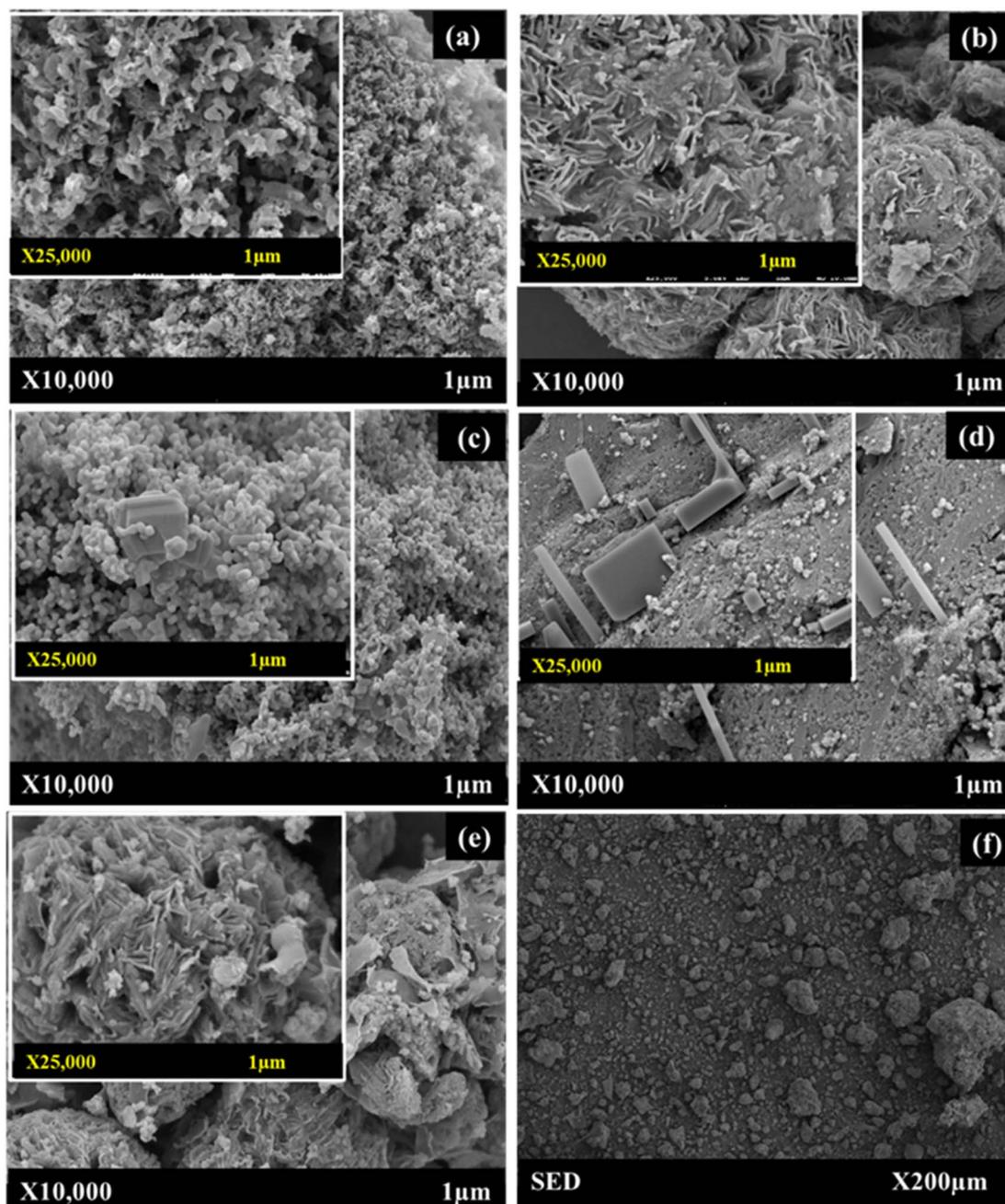
RSC Advances Paper

Fig. 6 HRSEM images of (a) bulk g-C_3N_4, (b) S-doped g-C_3N_4, (c) cubical-shaped CuO NPs, (d) monoclinic-shaped ZrO_2 NPs, (e) SED image CuO/ZrO_2@S-doped g-C_3N_4 NCs at 1 μm, and (f) SED image CuO/ZrO_2@S-doped g-C_3N_4 NCs at ×200 μm.

CuO/ZrO_2@S-doped g-C_3N_4 NC is made up of three different types of morphological microspheres, including a thin straight bar, *i.e.* rod-shaped S, flower-shaped S-doped g-C_3N_4 (Fig. 6c and d), cubic-shaped CuO and monoclinic-shaped ZrO_2 NPs. These findings support the fact that CuO/ZrO_2@S-doped g-C_3N_4 NCs were successfully formed. This form of hybrid hetero-structured composite enhances electron accumulation on the conduction band, sustaining electron flow and reducing the rate of electron–hole recombination.[50] The cubical-shaped CuO (Fig. 6c) and the monoclinic-shaped ZrO_2 (Fig. 6d) NPs exhibit a morphology that shows the particles aggregated together to form irregular shapes and variable packing densities of CuO/ZrO_2@S-doped g-C_3N_4 NC (Fig. 6e). Interestingly, the HR-SEM/SED analysis (Fig. 6a–f) additionally verified the presence of N, C, S, O, Cu, and Zr elements within the CuO/ZrO_2@S-doped g-C_3N_4 NCs, providing evidence for the likely presence of CuO and ZrO_2 nanoparticles, which was challenging to confirm through the XRD study. Such heterostructures are important to enhance electron flow and reduce the recombination rate, which is favourable for catalytic reduction, photocatalytic degradation of molecules and electrochemical processes.[50]
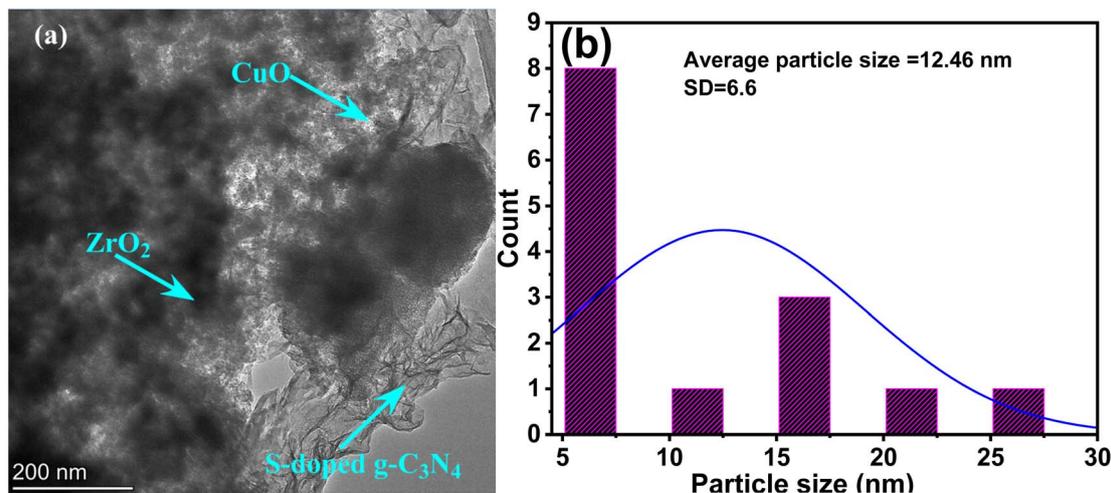
Paper

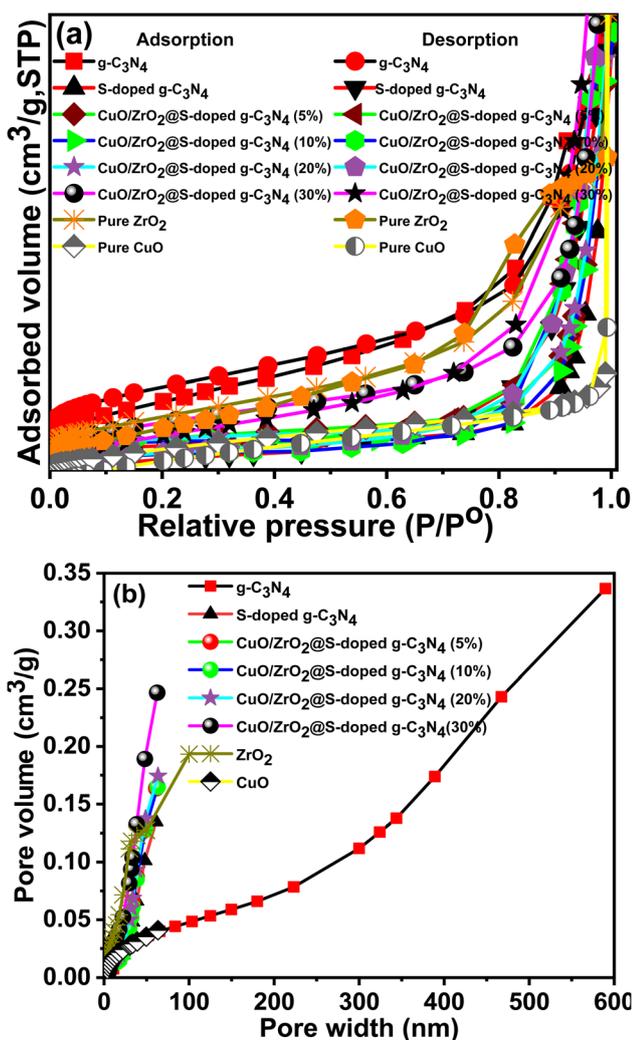**Fig. 7** (a) TEM and (b) HRTEM particle size distribution of CuO/ZrO$_2$@S-doped g-C$_3$N$_4$.

Fig. 8 (a) N$_2$ adsorption–desorption isotherms at 77 K, and (b) pore size distributions of pristine g-C$_3$N$_4$, S-doped g-C$_3$N$_4$, CuO/ZrO$_2$@S-doped g-C$_3$N$_4$ NCs, CuO and ZrO$_2$ NPs.

Fig. 9 X-ray photoelectron survey spectra for (a) g-C$_3$N$_4$, (b) S-doped g-C$_3$N$_4$, (c) CuO, (d) ZrO$_2$ and (e) CuO/ZrO$_2$@S-doped g-C$_3$N$_4$ NCs.

To ascertain the existence of CuO and ZrO$_2$ NPs in the S-doped g-C$_3$N$_4$ substrate, TEM images were provided for ternary NCs CuO/ZrO$_2$@S-doped g-C$_3$N$_4$ (30%). Small NPs dominate the structure. The ZrO$_2$ NPs were covered by black coloured S-doped g-C$_3$N$_4$, and the small CuO NPs are seen in white colour (Fig. 7a). Even though it is difficult to determine the spotty diffraction rings of the selected area electron diffraction (SAED) pattern for CuO and ZrO$_2$ NPs, it is possible to differentiate the NPs constructing the composite on the TEM image (Fig. 7b). From the PL and XPS data, it can be concluded that the presence of CuO, ZrO$_2$ and S in the synthesized NCs showed surface defects. Here, particle size distribution analysis shows the sizes of the synthesized NCs found to be in the nanometre range (~4–30 nm), which aligns with the XRD analysis. In conclusion, the development of ternary NCs, which was challenging to see in the XRD investigation, is clearly visible in the TEM pictures and is consistent with the findings of HRSEM and XPS.

3.5 Brunauer–Emmett–Teller (BET) analysis

The BET (Brunauer–Emmett–Teller) method was used to measure the surface areas of the samples, and the pore sizes were derived from the pore volume distribution curves using the BJH (Barrett–Joyner–Halenda) technique. For ternary NCs, the specific adsorption of N_2 as well as the pore volume increased when the amount of CuO and ZrO_2 increased (see Fig. 8a and b). The sorption of ternary samples exhibits type IV isotherms with hysteresis loops (Fig. 8a), which mostly corresponds to the mesoporous nature of materials.

The use of S, CuO and ZrO_2 NPs resulted in increased surface area and pore volume, with profound decrease in pore diameter as compared to g-C_3N_4 (Fig. 8b). Thus, when the amount of CuO and ZrO_2 is 30%, the surface area increased to 46.5 m^2 g^{-1} as compared to 28.2 m^2 g^{-1} in CuO/ZrO_2@S-doped g-C_3N_4 (5%). As shown in Table S1,† the CuO/ZrO_2@S-doped g-C_3N_4 NCs' surface area showed an increase in specific surface area with decrease in crystallite size, and profound change in pore volume.
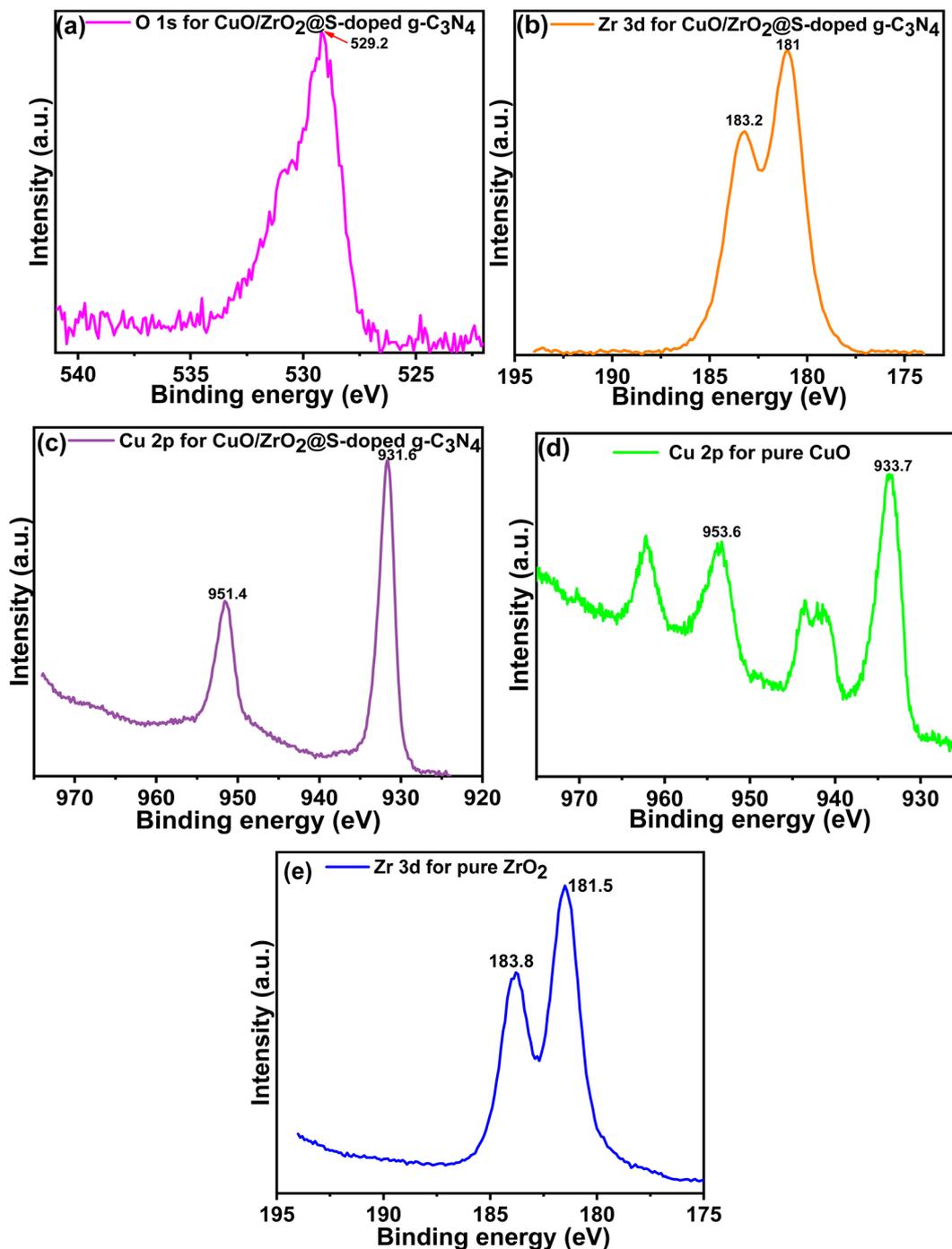

Fig. 10 High-resolution spectra of (a) O 1s, (b) Zr 3d, (c) Cu 2p of CuO/ZrO_2@S-doped g-C_3N_4 NC, and high-resolution spectra for (d) Cu 2p of pure CuO and (e) Zr 3d of pure ZrO_2.

© 2025 The Author(s). Published by the Royal Society of Chemistry

3.6 X-ray photoelectron spectroscopy (XPS) analysis

XPS was employed to confirm the oxidation states of CuO and ZrO_2. The survey spectrum of g-C_3N_4 revealed the composition of carbon and nitrogen exclusively (Fig. 9). The observed peaks at 288.1 eV and 398.7 eV correspond to C 1s and N 1s in g-C_3N_4, respectively.[51] These results are in good agreement with reported values for bonds in g-C_3N_4.[8,10,30] In the C 1s region of the three nanocomposites, there are peaks observed at 284.6 eV for g-C_3N_4.[51] Similar C 1s peaks were also observed for S-doped g-C_3N_4 (Fig. 9b) and CuO/ZrO_2@S-doped g-C_3N_4 (Fig. 9e). These peaks were previously assigned to S-doped g-C_3N_4, sp^2-bonded carbon (N=C=N), and π-excitation, respectively.[52] The S-doped g-C_3N_4 nanocomposite reveals distinct peaks for C 1s and N 1s, with binding energies similar to those of pure g-C_3N_4. Sulphur (S), however, is not observed, likely due to its low concentration, which is below the detectable range of the analytical instrument used. The survey spectra for CuO/ZrO_2@S-doped g-C_3N_4 nanocomposites confirm the presence of core elements, including C 1s, N 1s, Cu 2p, O 1s, and Zr 3d, indicating a substantial interaction between CuO, ZrO_2, and S-doped g-C_3N_4.[8,10,30]

CuO/ZrO_2@S-g-C_3N_4 NCs are depicted in Fig. 10. The high-resolution spectra of O 1s (Fig. 10a) reveal two distinct peaks. The low binding energy peak at 529.2 eV is attributed to lattice oxygen in Zr–O,[8,48,53] while the higher binding energy peak at 530.5 eV arises from the lattice oxygen of Cu–O.[54] Additionally, the O 1s signal at 529.2 eV is assigned to Zr–O bonds associated with O^{2-} ions in monoclinic ZrO_2.[8,55] Fig. 10b exhibits the Zr $3d_{5/2}$ and Zr $3d_{3/2}$ peaks of the CuO/ZrO_2@S-doped g-C_3N_4 NCs,

showing peaks at 183.3 eV and 181 eV, respectively. These peaks correspond to the Zr 3d spin–orbit split peaks, with previous studies assigning the peaks around 184.1 eV and 181.7 eV to Zr $3d_{5/2}$ and Zr $3d_{3/2}$, respectively.[8,55]

Fig. 10c shows the presence of a Cu–O bond in CuO/ZrO_2@S-doped g-C_3N_4, with the spin–orbit split peaks at 931.6 eV for Cu $2p_{3/2}$ and 951.4 eV for Cu $2p_{1/2}$.[41] Notably, these peaks are shifted compared to those observed for pure CuO (Fig. 10d), 953.6 eV and 933.7 eV, respectively. The Zr $3d_{5/2}$ and Zr $3d_{3/2}$ peaks of pure ZrO_2 (Fig. 10e) are observed at 183.8 eV and 181.5 eV, respectively, indicating peak-shifting upon incorporation of CuO in CuO/ZrO_2@S-doped g-C_3N_4 (Fig. 10c). XPS, therefore, confirms the presence of nitrogen, carbon, copper, oxygen and zirconium elements in the CuO/ZrO_2@S-doped g-C_3N_4 NC.[56]

3.7 Electrochemical behaviour of BPA at carbon paste-modified electrodes

BPA was employed as a model pollutant to evaluate the sensor capabilities of the synthesized NCs. The Carbon Paste Electrode (CPE) was utilized to assess the sensing performance of ternary NCs for BPA detection. Electrochemical studies were conducted on various modified electrodes, including g-C_3N_4/CPE, S-doped g-C_3N_4/CPE, CuO/ZrO_2@S-doped g-C_3N_4 (30%)/CPE, and the bare CPE. Experiments were carried out using a BPA concentration of 0.1 nM, a scan rate of 50 mV s^{-1}, and a pH of 5. The results are depicted in Fig. 11. It was evident from the results that, except for the bare CPE, all the modified CPE electrodes exhibited well-defined cyclic voltammetry (CV) peaks indicative
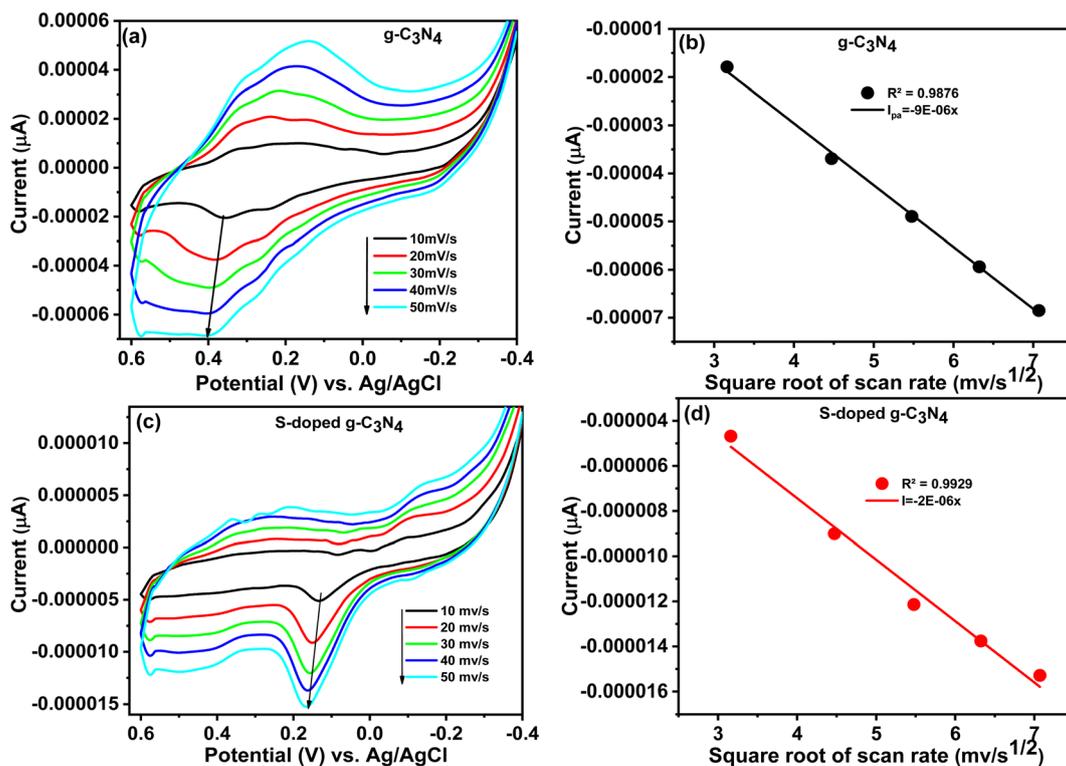

Fig. 11 CV curves of the interaction between BPA and (a) g-C_3N_4, (c) S-doped g-C_3N_4 at different scan rates; (b) and (d) show the relationship between peak current *vs.* square root of scan rate derived from the CV curves presented in (a) and (c), respectively. BPA = 0.1 nM and pH = 5.
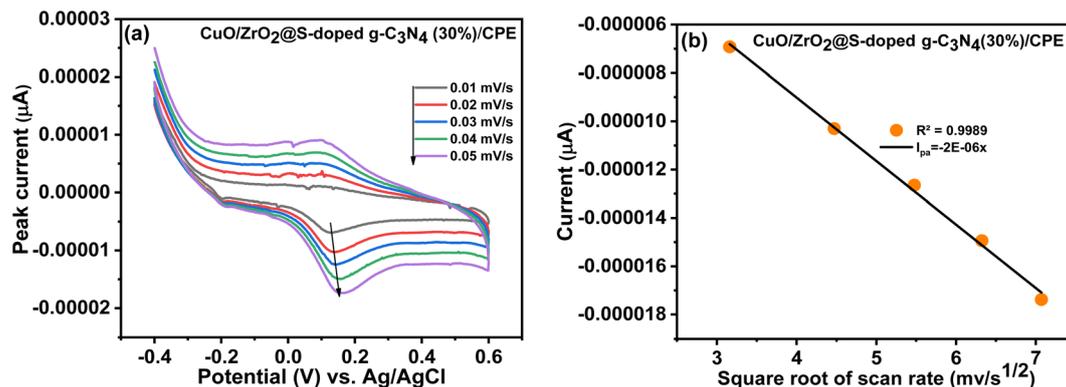
Fig. 12 CV voltammogram of (a) CuO/ZrO$_2$@S-doped g-C$_3$N$_4$ (30%) at different scan rates, (b) the linear relationship between peak current *vs.* square root of scan rate derived from the CV curves. BPA = 0.1 nM and pH = 5.

of various electron transfer capabilities. The bare CPE demonstrated limited electron transfer efficiency compared to the modified electrodes, mainly because its poor electrical conductivity hampers the electron transfer process for BPA on its surface. In contrast, the ternary CuO/ZrO$_2$@S-doped g-C$_3$N$_4$ (30%)/CPE electrodes exhibited distinct peak currents, signifying improved electron transfer performance, higher conductivity, and an increased surface area provided by the nanocomposites.

3.7.1 Effect of scan rate. To determine whether the electrochemical response mechanism was diffusion-controlled or not, experiments were conducted at varying scan rates (Fig. 11). An increase in peak current with the scan rate indicated enhanced electrocatalytic activity at the modified electrode's surface. In this context, the peak current increased linearly with the square root of the scan rate, suggesting that BPA oxidation at the modified CPE electrodes follows a diffusion-controlled process.[57] In comparing peak current intensity among the
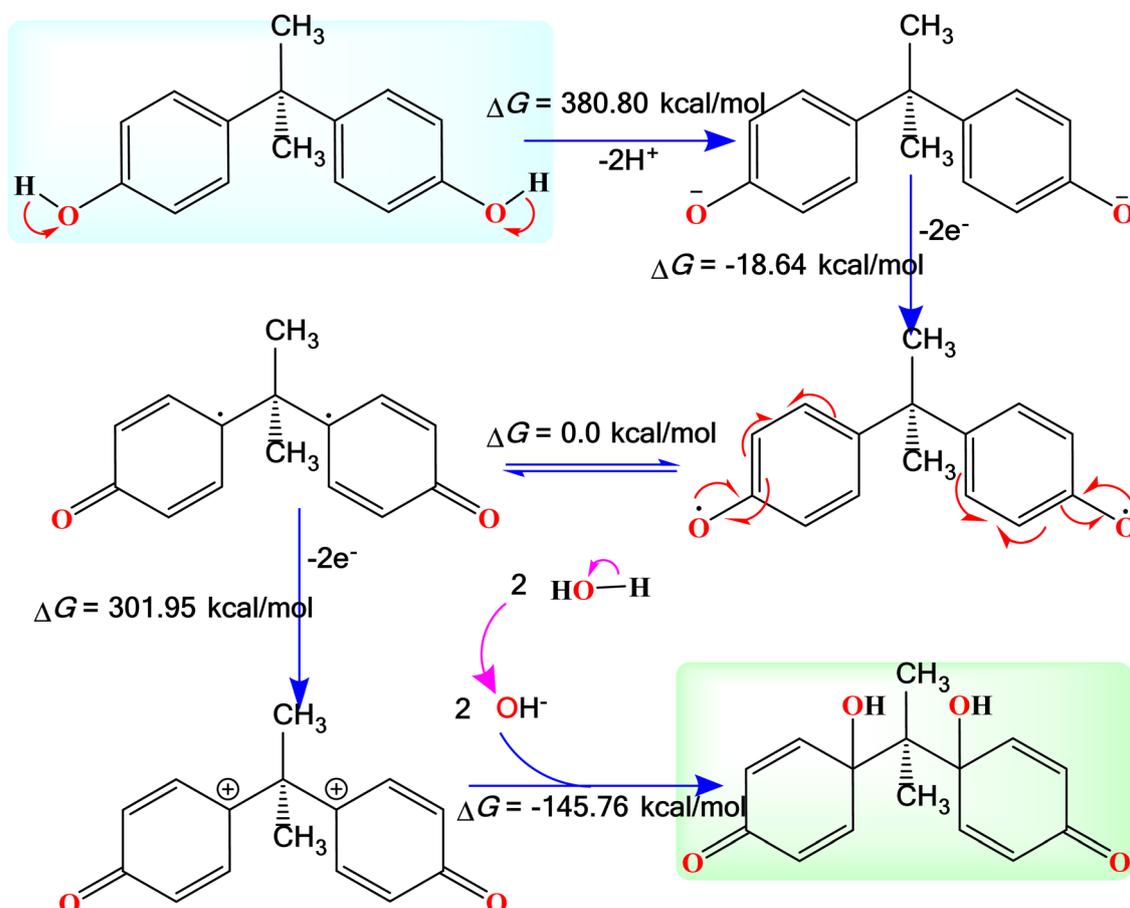

Fig. 13 Proposed electrochemical oxidation reaction mechanism of BPA at CuO/ZrO$_2$@S-doped g-C$_3$N$_4$ (30%) carbon paste electrode (CPE). The change in Gibbs free energies were calculated using B3LYP-D3/6-311++G(d,p).

modified electrodes, the ternary NC CuO/ZrO$_2$@S-doped g-C$_3$N$_4$ (30%)/CPE exhibits the highest peak current of -1.152×10^{-5} A at a potential of 0.166 V. The slope of the CuO/ZrO$_2$@S-doped g-C$_3$N$_4$ (30%)/CPE curve suggests that electron transfer is more rapid at CuO/ZrO$_2$@S-doped g-C$_3$N$_4$ (30%) than at the pristine g-C$_3$N$_4$/CP and S-doped g-C$_3$N$_4$/CP electrodes.[3]

3.7.2 Effect of concentration of bisphenol A. The quantitative chemical analysis potential of the modified electrodes was assessed by examining the relationship between anodic current and BPA concentration. Electrochemical measurements were performed on the modified CPEs across various BPA concentrations, with a scan rate of 50 mV s^{-1} over a potential range from -0.5 V to 0.9 V (Fig. 12). The modified CPE exhibited a stable response for BPA detection. Cyclic voltammetry (CV) cycles displayed small anodic peaks at the CuO/ZrO$_2$@S-doped g-C$_3$N$_4$ (30%)/CPE, indicating reliable electrochemical activity. Generally, comparing with other previously reported results[58] the CuO/ZrO$_2$@S-doped g-C$_3$N$_4$ (30%)/CPE system demonstrated good electrocatalytic performance, achieving reproducibility with a 1.7 μM detection limit and 2.1 μM limit of quantification.

The oxidation process is a multistep electron-transfer process. As illustrated in Fig. 13, the oxidation of BPA involves the transfer of two electrons, meaning that two protons are involved in the electrochemical oxidation reaction of BPA.[5,57] The B3LYP calculated results indicate that the first step is an endergonic reaction. It was predicted that this is the main step that needs to be initiated by the NC, probably the rate determining step. The next step is an exergonic reaction with a change in Gibbs free energy of -18.64 kcal mol^{-1} which involves the transfer of two electrons to the electrode, forming a diradical species. The third step involves transfer of additional two electrons, forming a dicationic species. Once the dicationic species is formed, it then reacts with two OH$^-$ ions to form the final product with a change in Gibbs free energy of -145.76 kcal mol^{-1}.

4. Conclusions

This study developed a gas-templating method to achieve one-step synchronous nano-structuring of S-doped g-C$_3$N$_4$. The process utilizes bottom-placed (NH$_4$)$_2$SO$_4$ as both a bi-functional gas template and a doping agent, enabling the transformation of top-placed urea into S-doped g-C$_3$N$_4$ at 550 °C. As the urea precursor, hydrated copper nitride and hydrated zirconium oxychloride are inexpensive and easily available, while the synthesis method is facile. We thus synthesized a ternary CuO/ZrO$_2$@S-doped g-C$_3$N$_4$ NCs efficiently and successfully. The crystallite size of the generated NCs was confirmed to be in the nanometre range by using the XRD and TEM investigations. The findings from UV-Vis/DRS, and PL indicate that, compared to pristine samples, the ternary NCs showed the best electron–hole recombination rate and band gap energy. BET analysis of the pore size distribution in the samples revealed that most pores exhibit type IV adsorption isotherms and type H3 hysteresis loops, with sizes ranging from 2 to 50 nm. The combination of S-doped g-C$_3$N$_4$, CuO, and ZrO$_2$ creates materials with beneficial properties, including a large specific surface area, mesoporous structure for enhanced adsorption, controlled electron–hole recombination, lower band gap energy, and improved crystallinity. Additionally, the ternary nanocomposites effectively catalysed the electrochemical oxidation of BPA, outperforming both g-C$_3$N$_4$ and S-doped g-C$_3$N$_4$. This enhancement is primarily due to the inclusion of CuO and ZrO$_2$, which introduces larger number of photon-activated active sites on the CuO/ZrO$_2$@S-doped g-C$_3$N$_4$ surface. The size of photon-activated site was estimated based on a decrease in the intensity of photoluminescence, which indicates a higher number of photon-activated sites contributing to enhanced charge separation. In addition, the large surface area of the NCs also provides more exposure allowing more BPA molecules to interact with the modified sensor. The heterojunction structure minimizes charge carrier recombination, fine-tunes the band gap energy, and provides additional active sites, thereby significantly maximizing electrochemical oxidation efficiency for BPA. This study addresses existing gaps in the literature by employing low-cost, readily available materials and a cost-effective synthesis method. Our results demonstrate the potential for scalable applications of such nanocomposites for environmental remediation.

Data availability

All data related to this publication is available either in the main manuscript or its ESI.†

Author contributions

N. Alebachew, T. B. Demissie, H. C. A. Murthy and B. A. Gonfa designed and ran the experiments, analysed the data, and wrote the original draft; N. Alebachew, K. G. v. Eschwege, E. Coetsee, E. H. G. Langner, Jayadev, and B. H. Doreswamy ran the characterization experiments; T. B. Demissie, H. C. A. Murthy and B. A. Gonfa supervised the work, and all authors reviewed and edited the manuscript.

Conflicts of interest

The authors have no conflicts of interest to declare.

Acknowledgements

References

1 J. Xing, S. Zhang, M. Zhang and J. A. Hou, Critical Review of Presence, Removal and Potential Impacts of Endocrine Disruptors Bisphenol A, *Comp. Biochem. Physiol., Part C:Toxicol. Pharmacol.*, 2022, 109275.

2 A. Aker, R. E. R. McConnell, R. Loch-Caruso, S. K. Park, B. Mukherjee, Z. Y. Rosario, C. M. Vélez-Vega, G. Huerta-Montanez, A. N. Alshawabkeh and J. F. Cordero, Interactions between Chemicals and Non-Chemical Stressors: The Modifying Effect of Life Events on the Association between Triclocarban, Phenols and Parabens with Gestational Length in a Puerto Rican Cohort, *Sci. Total Environ.*, 2020, **708**, 134719.

3 A. L. T. Zheng and Y. Andou, Detection and Remediation of Bisphenol A (BPA) Using Graphene-Based Materials: Mini-Review, *Int. J. Environ. Sci. Technol.*, 2022, **19**(7), 6869–6888, DOI: **10.1007/s13762-021-03512-x.**

4 J. G. Hengstler, H. Foth, T. Gebel, P. J. Kramer, W. Lilienblum, H. Schweinfurth, W. Völkel, K. M. Wollin and U. Gundert-Remy, Critical Evaluation of Key Evidence on the Human Health Hazards of Exposure to Bisphenol A, *Crit. Rev. Toxicol.*, 2011, **41**(4), 263–291, DOI: **10.3109/10408444.2011.558487.**

5 Y. Xu, W. Lei, Y. Zhang, H. Fan, Q. Hao and S. Gao, Bamboo Fungus-Derived Porous Nitrogen-Doped Carbon for the Fast, Sensitive Determination of Bisphenol A, *J. Electrochem. Soc.*, 2017, **164**(5), B3043–B3048, DOI: **10.1149/2.0021705jes.**

6 J. Rajendran, T. S. Kannan, L. S. Dhanasekaran, P. Murugan, R. Atchudan, Z. A. ALOthman, M. Ouladsmane and A. K. Sundramoorthy, Preparation of 2D Graphene/MXene Nanocomposite for the Electrochemical Determination of Hazardous Bisphenol A in Plastic Products, *Chemosphere*, 2022, **287**(P2), 132106, DOI: **10.1016/j.chemosphere.2021.132106.**

7 Z. Z. Vasiljevic, M. P. Dojcinovic, J. D. Vujancevic, I. Jankovic-Castvan, M. Ognjanovic, N. B. Tadic, S. Stojadinovic, G. O. Brankovic and M. V. Nikolic, Photocatalytic Degradation of Methylene Blue under Natural Sunlight Using Iron Titanate Nanoparticles Prepared by a Modified Sol–Gel Method, *R. Soc. Open Sci.*, 2020, **7**(9), 200708.

8 Y. Ke, H. Guo, D. Wang, J. Chen and W. Weng, ZrO$_2$/g-C$_3$N$_4$ with Enhanced Photocatalytic Degradation of Methylene Blue under Visible Light Irradiation, *J. Mater. Res.*, 2014, **29**(20), 2473–2482, DOI: **10.1557/jmr.2014.276.**

9 D. Zhu and Q. Zhou, Nitrogen Doped g-C$_3$N$_4$ with the Extremely Narrow Band Gap for Excellent Photocatalytic Activities under Visible Light, *Appl. Catal., B*, 2021, **281**, 119474, DOI: **10.1016/j.apcatb.2020.119474.**

10 A. Mohammad, M. E. Khan and M. H. Cho, Sulfur-Doped-Graphitic-Carbon Nitride (S-g-C$_3$N$_4$) for Low Cost Electrochemical Sensing of Hydrazine, *J. Alloys Compd.*, 2020, **816**, 152522, DOI: **10.1016/j.jallcom.2019.152522.**

11 J. Zhang, Y. Zheng, H. Zheng, T. Jing, Y. Zhao and J. Tian, Porous Oxygen-Doped g-C$_3$N$_4$ with the Different Precursors for Excellent Photocatalytic Activities under Visible Light, *Materials*, 2022, **15**(4), 1391, DOI: **10.3390/ma15041391.**

12 R. You, H. Dou, L. Chen, S. Zheng and Y. Zhang, Graphitic Carbon Nitride with S and O Co doping for Enhanced Visible Light Photocatalytic Performance, *RSC Adv.*, 2017, **7**(26), 15842–15850, DOI: **10.1039/C7RA01036B.**

13 M. Chegeni, F. Goudarzi and M. Soleymani, Synthesis, Characterization and Application of V$_2$O$_5$/S-Doped Graphitic Carbon Nitride Nanocomposite for Removing of Organic Pollutants, *ChemistrySelect*, 2019, **4**(46), 13736–13745, DOI: **10.1002/slct.201903885.**

14 S. Zhang, C. Su, H. Ren, M. Li, L. Zhu, S. Ge, M. Wang, Z. Zhang, L. Li and X. Cao, *In Situ* Fabrication of g-C$_3$N$_4$/ZnO Nanocomposites for Photocatalytic Degradation of Methylene Blue: Synthesis Procedure Does Matter, *Nanomaterials*, 2019, **9**(2), 215, DOI: **10.3390/nano9020215.**

15 L. Li, Y. Hu, D. Deng, H. Song and Y. Lv, Highly Sensitive Cataluminescence Gas Sensors for 2-Butanone Based on g-C$_3$N$_4$ Sheets Decorated with CuO Nanoparticles, *Anal. Bioanal. Chem.*, 2016, **408**(30), 8831–8841, DOI: **10.1007/s00216-016-9906-0.**

16 X. Jia, R. Dai, Y. Sun, H. Song and X. Wu, One-Step Hydrothermal Synthesis of Fe$_3$O$_4$/g-C$_3$N$_4$ Nanocomposites with Improved Photocatalytic Activities, *J. Mater. Sci.: Mater. Electron.*, 2016, **27**(4), 3791–3798, DOI: **10.1007/s10854-015-4224-4.**

17 A. K. Sibhatu, G. K. Weldegebrieal, S. Sagadevan, N. N. Tran and V. Hessel, Photocatalytic Activity of CuO Nanoparticles for Organic and Inorganic Pollutants Removal in Wastewater Remediation, *Chemosphere*, 2022, **300**, 134623, DOI: **10.1016/j.chemosphere.2022.134623.**

18 L. Kumari, W. Li and D. Wang, Monoclinic Zirconium Oxide Nanostructures Synthesized by a Hydrothermal Route, *Nanotechnology*, 2008, **19**(19), 195602, DOI: **10.1088/0957-4484/19/19/195602.**

19 Y. Li, D. He, Z. Cheng, C. Su, J. Li and Q. Zhu, Effect of Calcium Salts on Isosynthesis over ZrO$_2$ Catalysts, *J. Mol. Catal. A: Chem.*, 2001, **175**(1–2), 267–275.

20 R. Zhang, X. Zhang and S. Hu, High Temperature and Pressure Chemical Sensors Based on Zr/ZrO$_2$ Electrode Prepared by Nanostructured ZrO$_2$ Film at Zr Wire, *Sens. Actuators, B*, 2010, **149**(1), 143–154, DOI: **10.1016/j.snb.2010.06.009.**

21 N. Najibi-Ilkhechi, B. Koozegar-Kaleji and E. Salahi, Effect of Heating Rate on Structural and Optical Properties of Si and Mg Co-Doped ZrO$_2$ ZrO$_2$ Nanopowders, *Opt. Quantum Electron.*, 2015, **47**(5), 1187–1195.

22 S. C. Yan, Z. S. Li and Z. G. Zou, Photodegradation Performance of g-C$_3$N$_4$ Fabricated by Directly Heating Melamine, *Langmuir*, 2009, **25**(17), 10397–10401.

23 X. Wang, K. Maeda, X. Chen, K. Takanabe, K. Domen, Y. Hou, X. Fu and M. Antonietti, Polymer Semiconductors for Artificial Photosynthesis: Hydrogen Evolution by Mesoporous Graphitic Carbon Nitride with Visible Light, *J. Am. Chem. Soc.*, 2009, **131**(5), 1680–1681, DOI: **10.1021/ja809307s.**

24 X. Bai, S. Yan, J. Wang, L. Wang, W. Jiang, S. Wu, C. Sun and Y. A. Zhu, Simple and Efficient Strategy for the Synthesis of a Chemically Tailored G-C₃N₄ Material, *J. Mater. Chem. A*, 2014, **2**(41), 17521–17529, DOI: 10.1039/c4ta02781g.

25 G. Zhang, J. Zhang, M. Zhang and X. Wang, Polycondensation of Thiourea into Carbon Nitride Semiconductors as Visible Light Photocatalysts, *J. Mater. Chem.*, 2012, **22**(16), 8083–8091, DOI: 10.1039/c2jm00097k.

26 S. Berhanu, H. Gebremariam and S. Chufamo, The g-C₃N₄@CdO/ZnO Ternary Composite: Photocatalysis, Thermodynamics and Acute Toxicity Studies, *Heliyon*, 2022, **8**(11), e11612, DOI: 10.1016/j.heliyon.2022.e11612.

27 C. Zhou, Y. Wu, X. Yan, J.-J. Wang, Q. Wang, D. Wang, X. Yuan, J. Pan and X. Cheng, Is CuO Suitable for Improving the Electrochemical Properties of g-C₃N₄?, *J. Nanosci. Nanotechnol.*, 2020, **20**(6), 3415–3423, DOI: 10.1166/jnn.2020.17483.

28 N. Mao, Investigating the Heteronjunction between ZnO/Fe₂O₃ and g-C₃N₄ for an Enhanced Photocatalytic H₂ Production under Visible-Light Irradiation, *Sci. Rep.*, 2019, **9**(1), 12383, DOI: 10.1038/s41598-019-48730-z.

29 H. Guo, Z. Shu, D. Chen, Y. Tan, J. Zhou, F. Meng and T. Li, One-Step Synthesis of S-Doped g-C₃N₄ Nanosheets for Improved Visible-Light Photocatalytic Hydrogen Evolution, *Chem. Phys.*, 2020, **533**, 110714, DOI: 10.1016/j.chemphys.2020.110714.

30 N. Alebachew, H. C. A. Murthy, B. Abdissa, T. B. Demissie, K. G. von Eschwege, E. H. G. Langner and L. Coetsee-Hugo, Synthesis and Characterization of CuO@S-Doped g-C₃N₄ Based Nanocomposites for Binder-Free Sensor Applications, *RSC Adv.*, 2022, **12**(46), 29959–29974.

31 Z. Yang, Y. Sun, W. Wang, X. Yuan and P. Tian, Dual-Mechanism Study of Metal-Free g-C₃N₄ Catalysts for Advanced Oxidation Under Non-Photocatalytic Conditions, *Molecules*, 2025, **30**(2), 247, DOI: 10.3390/molecules30020247.

32 M. J. Frisch, G. W. Trucks, H. B. Schlegel, G. E. Scuseria, M. A. Robb, J. R. Cheeseman, G. Scalmani, V. Barone, G. A. Petersson, H. Nakatsuji, X. Li, M. Caricato, A. V. Marenich, J. Bloino, B. G. Janesko, R. Gomperts, B. Mennucci, H. P. Hratchian, J. V. Ortiz, A. F. Izmaylov, J. L. Sonnenberg, D. Williams-Young, F. Ding, F. Lipparini, F. Egidi, J. Goings, B. Peng, A. Petrone, T. Henderson, D. Ranasinghe, V. G. Zakrzewski, J. Gao, N. Rega, G. Zheng, W. Liang, M. Hada, M. Ehara, K. Toyota, R. Fukuda, J. Hasegawa, M. Ishida, T. Nakajima, Y. Honda, O. Kitao, H. Nakai, T. Vreven, K. Throssell, J. A. Montgomery, J. E. Peralta, F. Ogliaro, M. J. Bearpark, J. J. Heyd, E. N. Brothers, K. N. Kudin, V. N. Staroverov, T. A. Keith, R. Kobayashi, J. Normand, K. Raghavachari, A. P. Rendell, J. C. Burant, S. S. Iyengar, J. Tomasi, M. Cossi, J. M. Millam, M. Klene, C. Adamo, R. Cammi, J. W. Ochterski, R. L. Martin, K. Morokuma, O. Farkas, J. B. Foresman and D. J. Fox, *Gaussian 16 Revision C-01*, 2016.

33 A. D. Becke, Density-Functional Thermochemistry. III. The Role of Exact Exchange, *J. Chem. Phys.*, 1993, **98**, 5648–5652, DOI: 10.1063/1.464913.

34 C. Lee, W. Yang and R. G. Parr, Development of the Colle-Salvetti Correlation-Energy Formula into a Functional of the Electron Density, *Phys. Rev. B: Condens. Matter Mater. Phys.*, 1988, 85–789.

35 P. J. Stephens, F. J. Devlin, C. F. Chabalowski and M. J. Frisch, *Ab Initio* Calculation of Vibrational Absorption and Circular Dichroism Spectra Using Density Functional Force Fields, *J. Phys. Chem.*, 1994, **98**, 11623–11627.

36 R. Krishnan, J. S. Binkley, R. Seeger and J. A. Pople, Self-Consistent Molecular Orbital Methods. XX. A Basis Set for Correlated Wave Functions, *J. Chem. Phys.*, 1980, **72**, 650–654, DOI: 10.1063/1.438955.

37 J. Antony and S. Grimme, Density Functional Theory Including Dispersion Corrections for Intermolecular Interactions in a Large Benchmark Set of Biologically Relevant Molecules, *Phys. Chem. Chem. Phys.*, 2006, **8**, 5287–5293, DOI: 10.1039/b612585a.

38 J. Liu, T. Zhang, Z. Wang, G. Dawson and W. Chen, Simple Pyrolysis of Urea into Graphitic Carbon Nitride with Recyclable Adsorption and Photocatalytic Activity, *J. Mater. Chem.*, 2011, **21**(38), 14398, DOI: 10.1039/c1jm12620b.

39 K. Wang, Q. Li, B. Liu, B. Cheng, W. Ho and J. Yu, Sulfur-Doped g-C₃N₄ with Enhanced Photocatalytic CO₂-Reduction Performance, *Appl. Catal., B*, 2015, **176**, 44–52, DOI: 10.1016/j.apcatb.2015.03.045.

40 L. Bai, H. Huang, S. Yu, D. Zhang, H. Huang and Y. Zhang, Role of Transition Metal Oxides in g-C₃N₄-Based Heterojunctions for Photocatalysis and Supercapacitors, *J. Energy Chem.*, 2022, **64**, 214–235, DOI: 10.1016/j.jechem.2021.04.057.

41 J. Kavil, P. M. Anjana, D. Joshy, A. Babu, G. Raj, P. Periyat and R. B. Rakhi, g-C₃N₄/CuO and g-C₃N₄/Co₃O₄ Nanohybrid Structures as Efficient Electrode Materials in Symmetric Supercapacitors, *RSC Adv.*, 2019, **9**(66), 38430–38437, DOI: 10.1039/C9RA08979A.

42 J. Zhu, P. Xiao, H. Li and S. A. C. Carabineiro, Graphitic Carbon Nitride: Synthesis, Properties, and Applications in Catalysis, *ACS Appl. Mater. Interfaces*, 2014, **6**(19), 16449–16465, DOI: 10.1021/am502925j.

43 S. Cao, J. Low, J. Yu and M. Jaroniec, Polymeric Photocatalysts Based on Graphitic Carbon Nitride, *Adv. Mater.*, 2015, **27**(13), 2150–2176, DOI: 10.1002/adma.201500033.

44 M.-H. H. Vu, M. Sakar, C.-C. C. Nguyen and T.-O. O. Do, Chemically Bonded Ni Cocatalyst onto the S Doped G-C₃N₄ Nanosheets and Their Synergistic Enhancement in H₂ Production under Sunlight Irradiation, *ACS Sustain. Chem. Eng.*, 2018, **6**(3), 4194–4203, DOI: 10.1021/acssuschemeng.7b04598.

45 R. López and R. Gómez, Band-Gap Energy Estimation from Diffuse Reflectance Measurements on Sol–Gel and Commercial TiO₂: A Comparative Study, *J. Sol-Gel Sci. Technol.*, 2012, **61**(1), 1–7, DOI: 10.1007/s10971-011-2582-9.

46 A. Mitra, P. Howli, D. Sen, B. Das and K. K. Chattopadhyay, Cu₂O/g-C₃N₄ Nanocomposites: An Insight into the Band Structure Tuning and Catalytic Efficiencies, *Nanoscale*, 2016, **8**(45), 19099–19109, DOI: 10.1039/c6nr06837e.

47 N. Alebachew, H. C. A. Murthy, B. Abdissa, T. B. Demissie, K. G. von Eschwege, E. H. G. Langner and L. Coetsee-Hugo, Synthesis and Characterization of CuO@S-Doped g-C₃N₄ Based Nanocomposites for Binder-Free Sensor Applications, *RSC Adv.*, 2022, **12**(46), 29959–29974, DOI: **10.1039/D2RA04752G**.

48 N. Alebachew, H. C. A. Murthy, B. A. Gonfa, K. G. von Eschwege, E. H. G. Langner, E. Coetsee and T. B. Demissie, Nanocomposites with ZrO₂@S-Doped g-C₃N₄ as an Enhanced Binder-Free Sensor: Synthesis and Characterization, *ACS Omega*, 2023, **8**(15), 13775–13790, DOI: **10.1021/acsomega.2c08174**.

49 J. Zou, S. Wu, Y. Liu, Y. Sun, Y. Cao, J. P. Hsu, A. T. Shen Wee and J. Jiang, An Ultra-Sensitive Electrochemical Sensor Based on 2D g-C₃N₄/CuO Nanocomposites for Dopamine Detection, *Carbon*, 2018, **130**, 652–663, DOI: **10.1016/j.carbon.2018.01.008**.

50 M. A. Hanif, J. Akter, Y. S. Kim, H. G. Kim, J. R. Hahn and L. K. Kwac, Highly Efficient and Sustainable ZnO/CuO/g-C₃N₄ Photocatalyst for Wastewater Treatment under Visible Light through Heterojunction Development, *Catalysts*, 2022, **12**(2), 151, DOI: **10.3390/catal12020151**.

51 K. Li, M. Chen, L. Chen, S. Zhao, W. Xue, Z. Han and Y. Han, Synthesis of g-C₃N₄ Derived from Different Precursors for Photodegradation of Sulfamethazine under Visible Light, *Processes*, 2023, **11**(2), 528, DOI: **10.3390/pr11020528**.

52 J. Yuan, J. J. Zhang, M. P. Yang, W. J. Meng, H. Wang and J. X. Lu, Cuo Nanoparticles Supported on TiO₂ with High Efficiency for CO₂ Electrochemical Reduction to Ethanol, *Catalysts*, 2018, **8**(4), 171, DOI: **10.3390/catal8040171**.

53 E. Vijayakumar, M. Govinda Raj, M. G. Narendran, R. Preetha, R. Mohankumar, B. Neppolian and A. John Bosco, Promoting Spatial Charge Transfer of ZrO₂ Nanoparticles: Embedded on Layered MoS₂/g-C₃N₄ Nanocomposites for Visible-Light-Induced Photocatalytic Removal of Tetracycline, *ACS Omega*, 2022, **7**(6), 5079–5095, DOI: **10.1021/acsomega.1c06089**.

54 W. Zhang, H. Lei, S. Yao and H. Wang, Enhancement of Photoelectric Conversion Efficiency with Sulfur-Doped g-C₃N₄/TiO₂ Nanoparticles Composites in Dye-Sensitized Solar Cells, *J. Mater. Sci.: Mater. Electron.*, 2019, **30**(10), 9861–9871, DOI: **10.1007/s10854-019-01323-y**.

55 E. Vijayakumar, M. G. Raj, M. G. Narendran, R. Preetha, R. Mohankumar, B. Neppolian and A. J. Bosco, Promoting Spatial Charge Transfer of ZrO₂ Nanoparticles: Embedded on Layered MoS₂/g-C₃N₄ Nanocomposites for Visible-Light-Induced Photocatalytic Removal of Tetracycline, *ACS Omega*, 2022, **7**(6), 5079–5095, DOI: **10.1021/acsomega.1c06089**.

56 A. Verma, S. Kumar, W.-K. Chang and Y.-P. Fu, Bi-Functional Ag-CuₓO/GC₃N₄ Hybrid Catalysts for the Reduction of 4-Nitrophenol and the Electrochemical Detection of Dopamine, *Dalton Trans.*, 2020, **49**(3), 625–637, DOI: **10.1039/C9DT04309H**.

57 K. Kunene, M. Sabela, S. Kanchi and K. Bisetty, High Performance Electrochemical Biosensor for Bisphenol A Using Screen Printed Electrodes Modified with Multiwalled Carbon Nanotubes Functionalized with Silver-Doped Zinc Oxide, *Waste Biomass Valorization*, 2020, **11**(3), 1085–1096, DOI: **10.1007/s12649-018-0505-5**.

58 J. Cai, B. Sun, W. Li, X. Gou, Y. Gou, D. Li and F. Hu, Novel Nanomaterial of Porous Graphene Functionalized Black Phosphorus as Electrochemical Sensor Platform for Bisphenol A Detection, *J. Electroanal. Chem.*, 2019, **835**, 1–9, DOI: **10.1016/j.jelechem.2019.01.003**.